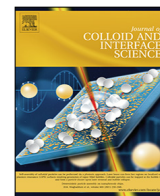




Contents lists available at ScienceDirect

Journal of Colloid and Interface Science

journal homepage: www.elsevier.com/locate/jcis

Oxygen vacancy-rich N-doped carbon encapsulated BiOCl-CNTs heterostructures as robust electrocatalyst synergistically promote oxygen reduction and Zn-air batteries



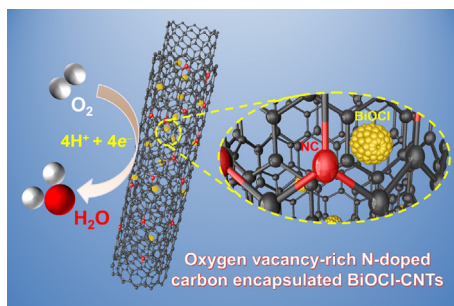
Xue Shao^a, Yuting Yang^a, Yi Liu^a, Puxuan Yan^a, Shuqing Zhou^a, Tayirjan Taylor Isimjan^{b,*}, Xiulin Yang^{a,*}

^aGuangxi Key Laboratory of Low Carbon Energy Materials, School of Chemistry and Pharmaceutical Sciences, Guangxi Normal University, Guilin 541004, China

^bSaudi Arabia Basic Industries Corporation (SABIC) at King Abdullah University of Science and Technology (KAUST), Thuwal 23955-6900, Saudi Arabia

GRAPHICAL ABSTRACT

An oxygen vacancy-rich N-doped carbon encapsulated BiOCl-CNTs catalyst is constructed by stepwise hydrothermal reaction, carbonization and etching conversion methods. The designed catalyst exhibits excellent electrocatalytic activity and stability in oxygen reduction reaction and zinc-air battery applications.



ARTICLE INFO

Article history:

Received 13 June 2021

Revised 28 August 2021

Accepted 30 August 2021

Available online 2 September 2021

Keywords:

N-doped carbon

BiOCl-CNTs

Synergistic effect

Oxygen reduction

Zn-air battery

ABSTRACT

The development of non-precious metal catalysts for oxygen reduction reactions (ORR) is vital for promising clean energy technologies such as fuel cells, and zinc-air batteries. Herein, we present a stepwise synthesis of N-doped and carbon encapsulated BiOCl-CNTs heterostructures. Electrochemical ORR studies show that the optimized catalyst has a high half-wave potential ($E_{1/2}$) of 0.85 V (vs. RHE), large limiting current density (-5.34 mA cm^{-2} @ 0.6 V) in alkaline medium, and nearly perfect $4e^-$ reduction characteristics, even surpassing commercial Pt/C. Meanwhile, the catalyst has exceptional durability (above 97.5 % after 40000 s) and strong resistance towards methanol poisoning. The good ORR activity also results in high-performance zinc-air batteries with a specific capacity (724 mAh g^{-1} @ 10 mA cm^{-2}), a high open-circuit potential of 1.51 V and a peak power density of 170.7 mW cm^{-2} , as well as an ultra-long charge-discharge cycle stability (155 h), comparable with the Pt/C catalyst. The catalytic mechanism reveals that the excellent electrocatalytic performance originates from the synergistic effect of N doping, oxygen vacancies, and BiOCl sites.

© 2021 Elsevier Inc. All rights reserved.

* Corresponding authors.

E-mail addresses: isimjant@sabic.com (T. Taylor Isimjan), xlyang@gxnu.edu.cn (X. Yang).

<https://doi.org/10.1016/j.jcis.2021.08.210>

0021-9797/© 2021 Elsevier Inc. All rights reserved.

1. Introduction

The massive energy consumption triggering a fossil-fuel-based energy crisis leads to an increasing interest in renewable clean

energy storage and conversion systems [1]. Among the various energy conversion devices, the Zn-air battery has attracted considerable attention because of its safety, high energy density, and commercial viability [2,3]. Zn-air batteries are made of cheap materials (Zn, KOH and carbon) with a high theoretical energy density of 1084 Wh kg⁻¹ [4]. Moreover, they are safe and easy to recycle. The Zn resource in the earth is 300 times higher than that of Li. Therefore, it does not pose any threat of resource limitation even if all the cars in the entire world are powered by Zn-air batteries. Most importantly, the cost of Zn in the Zn-air batteries only added 4–5 € kWh⁻¹ overall cost [5]. However, there are many challenges in developing effective electrocatalysts for high-performance Zn-air cells [6]. An ORR catalyst is the crucial part of the rechargeable Zn-air batteries that determine their capacity, cycling stability, and lifetime. However, the sluggish four-electron path and high overpotential are two major hurdles of developing a high-performance ORR catalyst to enhance the overall properties of the Zn-air battery [7,8]. The noble metals (Pt, Ir, and Ag) and their oxides are reckoned as the most active catalyst for ORR. However, the low natural abundance, poor durability, high cost and poor methanol tolerance limit their extensive application [9]. Hence, it is necessary to develop inexpensive ORR with higher catalytic efficiency, durability, and the ability to tolerate poisonous species to promote the utilization of Zn-air batteries [10,11].

The common strategies of preparing the high-performance transition-metal-based ORR catalysts follow three main pathways, including heteroatom doping (N, B, S, P) [12–15], increasing the oxygen vacancies [16], and improving the graphitization [17]. For instance, Chen et al. reported the preparation of high activity ORR electrocatalyst by N-doped carbon-coupled FeNi₃ composites [18]. Lu et al. demonstrated a high performance ORR catalyst composed of Co, N co-doped carbon nanotube with carbon wrapped CoS_x core [19]. They both claimed that coating N-doped carbon nanotubes on metal nanocatalysts not only guarantee the high-current density but also prevents the catalyst aggregation thereof resulting in better ORR performance. In addition, creating a hierarchical porous structure accelerates the interfacial electron transfer and mass diffusion [20]. For example, an N-doped carbon matrix linked by carbon nanotubes was reported to enhance the interface conductivity of the carrier and realize electron transfer to the active site in the ORR process [21]. The high-performance transition metal ORR catalyst is generally based on Co, Fe, and Ni [22,23]. On the other hand, the main group metals such as Mg, Al, and Bi are known as being catalytically inactive, since they do not have required host-orbitals that are crucial for the catalytic cycles that are especially important to the ORR process [1,24]. Interestingly, Zhang et al. recently developed a BiN₄ single site of high selectivity and activity catalyst for CO₂ reduction using the bismuth-based metal-organic framework (Bi-MOF) template. DFT study illustrates that the unique intrinsic properties of BiN₄/C catalyst resulted in low Gibbs free energy for *COOH formation lowers onset potential for CO₂ reduction to CO and eventually leads to better performance [25]. Moreover, Wei et al. reported a single crystal bismuth halide oxide that improves the overall electrocatalytic activity due to its unique layered crystal structure. The loading and growth orientations of the BiOCl nanosheets change the self-induced internal electric field to regulate the charge carriers' behaviors. Thus it improves the photoelectric properties of the heterojunction photodetectors. [26]. In light of the above findings, we anticipate when Bi is incorporated into N-doped carbon by heat treatment to form a composite material with better conductivity. Also, the oxygen vacancy significantly reduces the energy barriers against ORR in the reaction pathways [27]. As a result, the synergy between the higher conductivity induced better charge transfer, and the abundant oxygen vacancies is the key for high ORR activity.

In this work, a high-performance Bi-based NC@BiOCl-CNTs catalyst was developed through a controllable hydrothermal reaction, together with carbonization and etching conversion methods. The NC@BiOCl-CNTs catalysts exhibit high catalytic performance, including onset and half-wave (E_{1/2}) potentials of 0.98 V and 0.85 V (vs. RHE, see Fig. S1 for RHE calibration), respectively. As a Zn-air cathode material, NC@BiOCl-CNTs catalyst exhibit excellent lasting stability (155 h) and power density (170.7 mW cm⁻²) by comparison with precious metal Pt/C catalyst (44 h, 129.6 mW cm⁻²). Our study indicates that melamine is beneficial to increasing active sites, which is in total agreement with the literature report [28]. Besides, the conductive CNTs improve the charge transfer, and the oxygen-containing functional groups on the carbon nanotubes act as a binder in anchoring the BiOCl particles to the carbon matrix [29].

2. Experimental section

2.1. Materials

Bismuth nitrate pentahydrate (Bi(NO₃)₃·5H₂O, ≥99.0%), melamine (C₃H₆N₆, 99%), dopamine hydrochloride ((HO)₂C₆H₃CH₂NH₂·HCl, 98%), poly(ethylene glycol)-*block*-poly(propylene glycol)-*block*-poly(ethylene glycol) (F127, MW ~ 12600), 2-aminoterephthalic acid (C₈H₇O₄, >98%), nitric acid (HNO₃, 65 ~ 68%), hydrochloric acid (HCl, 36 ~ 38%), N,N-dimethylformamide (HCON(CH₃)₂, ≥99.5%), potassium hydroxide (KOH, 90%), acetone (CH₃COCH₃, ≥99.5%), anhydrous ethanol (C₂H₅OH). All reagents are analytical grade and can be used directly without further purification. Carbon nanotubes (CNTs, >95%, outer diameter: 10–20 nm, length: 10–30 μm) was purchased from Aladdin. Nafion solution (5 wt%) and commercial Pt/C (J-M, 20 wt% Pt) were purchased from Alfa Aesar. Deionized water was used in all experiments.

2.2. Synthesis of acid-treated CNTs

First, 30 mL concentrated HNO₃ and 200 mg CNTs were mixed in a three-neck round bottom, and the mixture was continuously stirred in an oil bath at 90 °C for 4 h. After cooling down to room temperature, the mixture was diluted, centrifuged, washed (pH = 7), and dried to obtain the pretreated CNTs.

2.3. Synthesis of PDA@Bi-CNTs

Typically, 0.06 g of pretreated carbon nanotubes, 6 mmol of Bi(NO₃)₃·5H₂O, 1 g of F127, and 1.5 mmol of 2-amino-terephthalic (BDC-NH₂) were one-pot dissolved in 60 mL DMF solution. After the bismuth nitrate was completely dissolved and carbon nanotubes were ultrasonically dispersed in the mixed solution, the black mixture was sealed in an autoclave, heated to 180 °C, and kept for 8 h. After cooling to room temperature, the obtained brown powder was ultrasonically dispersed into 60 mL acetone solution containing 20 mL 10 mg mL⁻¹ dopamine-acetone hydrochloride solution. Then, the mixture was slowly heated to 180 °C, and kept for 8 h. After cooling, it was centrifuged, rinsed with deionized water and dried overnight at 60 °C. Finally, the product was obtained and identified as PDA@Bi-CNTs, where PDA represents polydopamine. As a control, PDA@Bi (without adding CNTs) was prepared by a similar method as mentioned above.

2.4. Preparation of NC@Bi-CNTs

To prepare a series of NC@Bi-CNTs-T (T = 900, 950 and 1000 °C) catalysts, 100 mg PDA@Bi-CNTs and melamine (mass ratio 1/10)

are uniformly ground and transferred to a ceramic container. Finally, the NC@Bi-CNTs was carbonized at 950 °C in argon for 2 h with a heating rate of 5 °C min⁻¹. The samples obtained are denoted according to their annealing temperature as NC@Bi-CNTs-900, -950 and -1000, respectively.

As a control, NC@Bi and N-CNTs were also prepared at 950 °C by the similar method described above, where PDA@Bi and CNTs were used instead of PDA@Bi-CNTs, respectively. In addition, C@Bi-CNTs (without adding melamine) was synthesized by a similar method.

2.5. Preparation of NC@BiOCl-CNTs

The NC@Bi-CNTs was further immersed in aqua regia (HNO₃/HCl = 1/3) for 12 h, and rinsed with abundant DI-water to be neutral. The resulted product was named as NC@BiOCl-CNTs. As a control, NC@BiOCl and C@BiOCl-CNTs were synthesized by a similar method, with NC@Bi and C@Bi-CNTs as the precursors, respectively.

2.6. Characterization

Scanning electron microscope (SEM) (FEI Quanta 200 FEG) and transmission electron microscope (TEM) (TF20, JEOL 2100F) with elemental mapping were used to characterize the morphology and microscopic structure of the catalyst. X-ray powder diffraction (XRD, Rigaku, D/Max-3C, Japan, scanning rate: 5° min⁻¹) and confocal Raman spectroscopy (Renishaw, England) were used to characterize the crystal structure of the samples. The chemical states of the catalyst were analyzed by X-ray photoelectron spectroscopy (XPS, ESCALAB 250Xi). Brunauer–Emmett–Teller (BET) and *t*-Plot methods were used to measure the specific surface area and pore size distribution, respectively. Elemental composition of the samples was determined by inductively coupled plasma-atomic emission spectrometry (ICP-AES). The nitrogen content in the catalytic material was measured and analyzed using an elemental analyzer (PE2400 II).

2.7. Electrode fabrication

In this work, the rotating ring disk electrode (RRDE, disk area = 0.247 cm²) was polished and selected as the working electrode. For the preparation of catalyst ink: 4 mg black powder was weighed and dispersed into 1 mL 5 wt% Nafion solution (the volume ratio of isopropanol/water = 1/3). Catalyst ink droplets of 19.6 μL were added to the surface of the polished RRDE with a pipette-gun and dried in a natural environment. The catalyst loading and Pt/C loading on the working electrode were 0.318 and 0.081 mg cm⁻², respectively.

The electrocatalytic ORR performance is obtained by rotating ring-disk electrodes in a three-electrode system, while the performance of the zinc-air battery is achieved by a home-made zinc-air battery device (see supporting information for details). Each measurement was repeated at least three times to ensure the reproducibility of the results.

3. Results and discussion

3.1. Synthesis and crystallinity analysis

The NC@BiOCl-CNTs hybrid material is constructed through a controllable four-step process, which involves Bi NPs reduction on CNT surface, PDA packaging, nitrogen doping, and BiOCl formation by aqua regia etching (Fig. 1a). In the first step, BDC-NH₂ is used as a reducing agent, and PVP is used as a modifier to reduce Bi NPs on CNT surface at high temperature to form Bi-CNTs

(Fig. 1b). XRD pattern shows that the Bi NPs matches the hexagonal-close-packed (hcp) metallic Bi (JCPDS: 44–1246) [30]. Second, the dopamine monomer polymerizes at high temperatures and wraps on the Bi-CNT surface to form PDA@Bi-CNTs [31]. Third, PDA@Bi-CNTs are carbonized at 950 °C, and melamine is used as a nitrogen source to form NC@Bi-CNTs (Fig. 1c and Fig. S2). Finally, after etching with aqua regia, most of the bare Bi NPs dissolve into the solution, and a small portion of the Bi NPs meshed by the carbon grid is transformed into BiOCl species, thereby obtaining NC@BiOCl-CNTs hybrid material (Fig. 1d). The clear four distinct characteristic peaks at 11.98°, 25.86°, 32.50°, and 33.45° are ascribed to the (001), (101), (110) and (102) crystal planes of BiOCl (JCPDS: 06–0249). Notably, when the hybrid material is subjected to continuous 20 cycles of CV treatment (0.05–1.15 V vs. RHE) (Fig. S3), the crystal structure of BiOCl does not change, implying that it has good ORR stability. Besides, three additional diffraction peaks appeared at 14.84°, 16.67°, and 22.77° after electrochemical treatment are corresponding to the hexagonal carbon (110), (002), and (120) crystal faces.

3.2. Microstructure and porosity analysis

Scanning electron microscopy (SEM) and transmission electron microscopy (TEM) were used to investigate the morphologies and microstructures of NC@Bi-CNTs and NC@BiOCl-CNTs. The surface of CNTs in NC@Bi-CNTs is decorated with dense particulate matters (Fig. 2a). After etching with aqua regia, the NC@BiOCl-CNTs surface becomes relatively smooth, due to the gradual dissolution of the Bi particles (Fig. 2b). The TEM image shows that some particulate materials are randomly distributed on the CNTs surface (Fig. 2c). The high-resolution TEM images demonstrate that a set of clear lattice fringes of 0.34 nm is typical C (002) crystal faces. The lattice spacing of 0.27 nm belongs to the (102) crystal faces of BiOCl (Fig. 2d–e) [32]. The selected area diffraction pattern (SAED) shows two sets of relatively distinctive diffraction rings index the (101) and (102) crystal planes of BiOCl that confirm the tetragonal structure (Fig. 2f). In addition, HAADF-STEM and corresponding element mappings appear that Bi, Cl, C, N, and O elements are uniformly distributed on the surface of NC@BiOCl-CNTs (Fig. 2g). The metal content of Bi in NC@BiOCl-CNTs was measured by ICP-AES (Table S1), and the result showed that the weight percentage of Bi was about 2.35 wt%.

Raman spectroscopy is an effective method to analyze the defect structure and graphitization degree of carbon materials. Generally, the intensity ratio of D-band (*sp*₃ carbon) and graphitic G-band (*sp*₂ carbon) (*I*_D/*I*_G) is used to evaluate the index of carbon disorders [33]. As shown in Fig. 3a, the NC@BiOCl-CNTs synthesized at 950 °C has the smallest *I*_D/*I*_G value (0.85) relative to the samples prepared at 900 °C (0.91) and 1000 °C (0.93), indicating that the samples prepared at 950 °C have higher graphitization degree and conductivity, thus facilitating electron transfer in the electrochemical ORR process [34]. Compared with C@BiOCl-CNTs (0.87) and NC@BiOCl (0.96), the doping of N element has little effect on the graphitization of hybrid materials, while the introduction of CNTs can greatly enhance the graphitization and conductivity of hybrid materials (Fig. 3b). Studies have shown that the graphitization degree of carbon and suitable N species contribute to ORR activity [35,36]. Table S2 summarizes the elemental analysis results of different materials, indicating that the NC@BiOCl-CNTs catalyst has the highest N content (1.98 wt%). According to previous reports, the N-doped component is chemically active that increases the more active sites, and changes the electronegativity of the adjacent C atom, thus enhancing the ORR intrinsic activity [37]. Moreover, BET measurement and related porosity analysis showed that NC@BiOCl-CNTs had a large specific surface area of

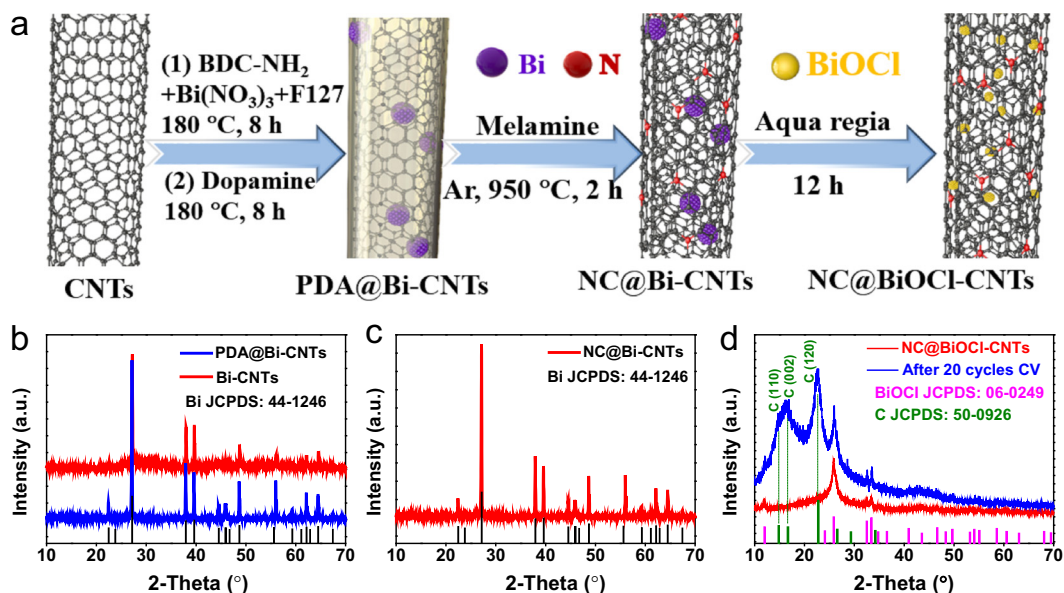


Fig. 1. (a) Schematic synthesis of NC@BiOCl-CNTs. XRD patterns of (b) PDA@Bi-CNTs and Bi-CNTs, (c) NC@Bi-CNTs, and (d) NC@BiOCl-CNTs before and after 20 cycles of electrochemical CV treatment.

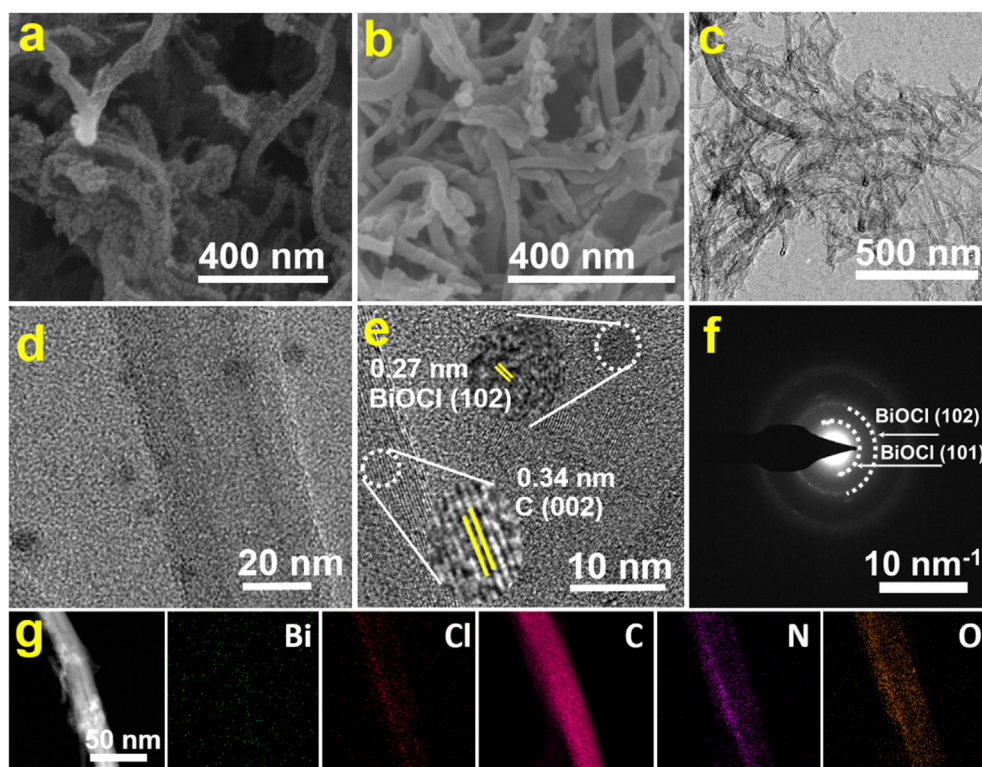


Fig. 2. SEM images of (a) NC@Bi-CNTs and (b) NC@BiOCl-CNTs. (c) TEM and (d, e) high-resolution TEM images of NC@BiOCl-CNTs. (f) SAED pattern of NC@BiOCl-CNTs. (g) HAADF-TEM image and corresponding elemental mappings of NC@BiOCl-CNTs.

$357.5 \text{ m}^2 \text{ g}^{-1}$ with an average pore diameter of 7.8 nm (inset) (Fig. 3c), indicating a mesopore dominated feature. This mesoporous feature with a high specific surface area can expose more active sites, and help solute transport and gas emission, thereby improving the ORR catalytic performance.

3.3. Chemical state analysis

The chemical valence states and bonding configurations of the synthesized catalysts were further studied by X-ray photoelectron spectroscopy (XPS). As displayed in Fig. S4a, NC@BiOCl-CNTs

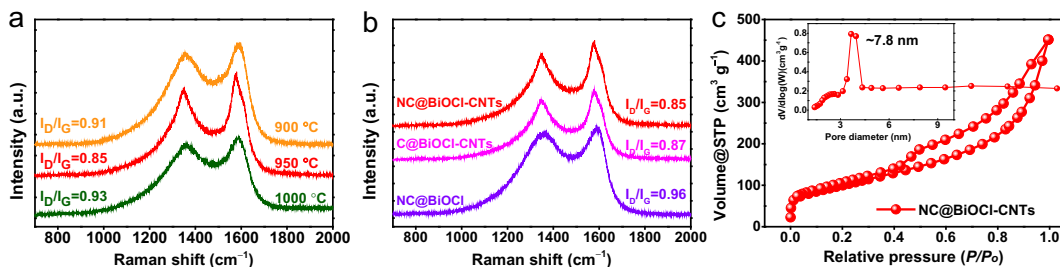


Fig. 3. Raman spectra of (a) NC@BiOCl-CNTs carbonized at 900, 950 and 1000 °C, and (b) different samples carbonized at 950 °C in Ar atmosphere. (c) N₂ adsorption-desorption isotherm with the inset pore size distribution of NC@BiOCl-CNTs.

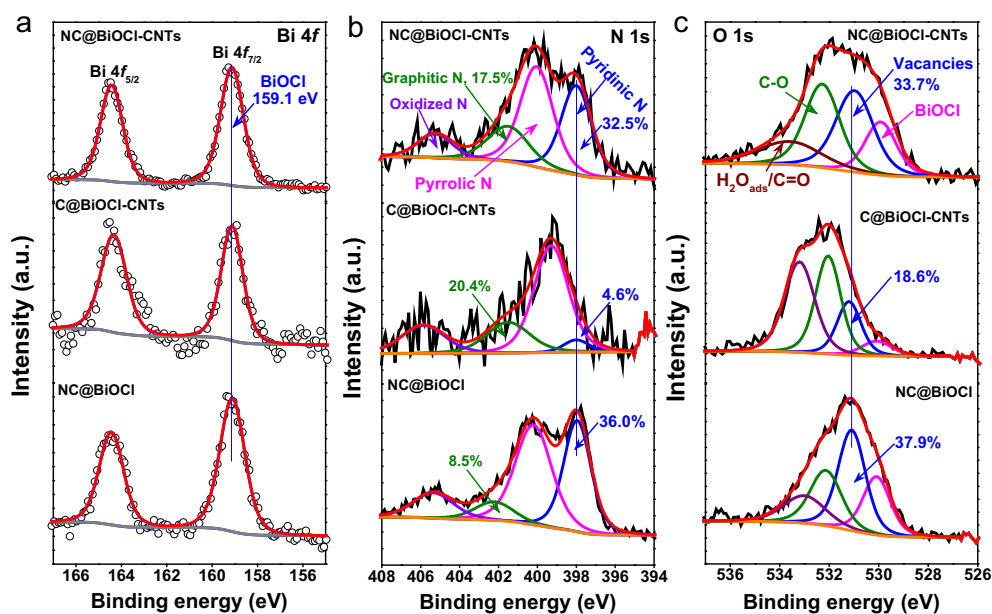


Fig. 4. Core-level XPS spectra of (a) Bi 4f, (b) N 1s and (c) O 1s regions from NC@BiOCl-CNTs, C@BiOCl-CNTs, and NC@BiOCl, respectively.

showed clear C, N, O, Cl and Bi peaks. The high-resolution C 1s signal of NC@BiOCl-CNTs is deconvoluted into four characteristic peaks of C=C (284.0 eV), C–C/C–N (284.8 eV), C–O (286.0 eV) and C=O (288.5 eV) (Fig. S4b) [38,39]. Fig. 4a shows high-resolution Bi 4f characteristic peaks of all composites, all of which can be deconvoluted into binding energies of 159.1 eV (Bi 4f_{7/2}) and 164.3 eV (Bi 4f_{5/2}) doublet attributable to typical BiOCl species [40].

The deconvolution of N 1s peaks of the catalyst can be divided into four parts (Fig. 4b). For instance, they are pyridinic N (400.0 eV), graphitic N (401.5 eV), and oxidized N (405.3 eV) [41,42], respectively. Many studies have proved that the electronic synergism between pyridinic N and graphitic N in N-doped carbon materials improves ORR catalytic activity in alkaline electrolytes [43,44]. For NC@BiOCl-CNTs catalyst, the ratio of pyridinic N is 32.5% (Fig. 4b) and similar to that of NC@BiOCl (36%). It is much higher than the integral area of C@BiOCl-CNTs (4.6%) according to the peak.

Similarly, the graphitic N content of NC@BiOCl-CNTs (17.5%) is similar to that of C@BiOCl-CNTs (pyridinic N: 20.4%) but significantly higher than that of NC@BiOCl (8.5%). On the whole, NC@BiOCl-CNTs have the optimized content of pyridinic N and graphitic N, which can regulate the charge redistribution on carbon materials to promote O₂ adsorption and reduce the energy barriers of O₂ hydrogenation, thus showing the improved performance of ORR [44]. Apart from the N-doped carbon matrix, O species are also critical to accelerating the ORR kinetics.

For core level XPS spectra of O 1s in Fig. 4c, there exist four types of characteristic peaks: 530.0, 531.1, 532.3, and 533.5 eV, which can correspond with lattice oxygen, oxygen vacancies, C–O, and adsorbed H₂O/C=O of BiOCl, respectively [45,46]. Upon previously reported literature results, abundant oxygen vacancies not only can enhance charge transfer but facilitate the dissociation of O₂, which can elevate ORR activity [47,48]. The oxygen vacancies are 33.7% and 37.9% in NC@BiOCl-CNTs and NC@BiOCl materials respectively, while C@BiOCl-CNTs only contain 18.6%, which illustrates that N doping promotes the formation of oxygen defects.

Besides, the chemical state's analysis of NC@Bi-CNTs intermediate has also been explored (Fig. S5). The high-resolution Bi 4f of NC@Bi-CNTs exhibits two signature peaks corresponding to metallic Bi and Bi oxides at binding energies of 158.8 and 160 eV [49,50]. Moreover, the N 1s and O 1s of NC@Bi-CNTs show a high fraction of pyridinic N (30.6%) and graphitic N (21.7%), as well as a high percentage of oxygen vacancies (33.2%), comparable with these of NC@BiOCl-CNTs.

3.4. Electrochemical ORR analysis

The ORR electrocatalytic activity of the optimized catalyst in 0.1 M KOH solution was evaluated by RRDE. The optimization of the calcination temperature is shown in Fig. S6. The results show that when the annealing temperature is 950 °C, the best NC@BiOCl-CNTs catalyst can be obtained. Therefore, if not explic-

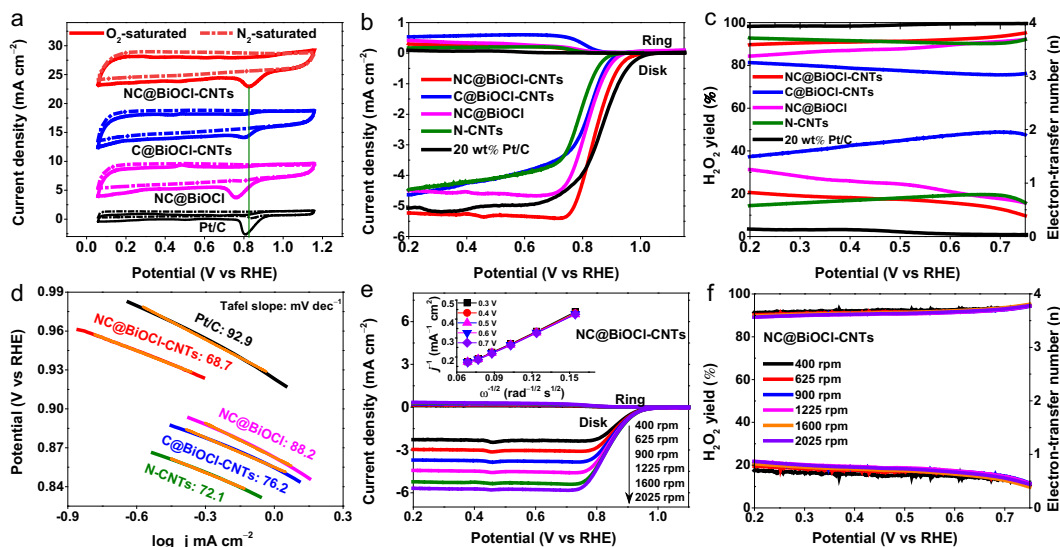


Fig. 5. Electrochemical performance of different catalysts. (a) CV and (b) LSV polarization curves of different catalysts in 0.1 M KOH solution. (c) H_2O_2 yield (%) and electron transfer number (n) calculated from RRDE test results. (d) Tafel plots for different catalysts. (e) LSV curves of NC@BiOCl-CNTs with various rotating speeds from 400 to 2025 rpm and the corresponding K-L plots (inset). (f) H_2O_2 yield (%) and electron transfer number (n) from various catalysts.

ity stated, the catalysts discussed below are prepared by calcination at 950 °C.

The catalyst activity of NC@BiOCl-CNTs and the comparative catalyst in N_2 - or O_2 -saturated alkaline solution was first investigated by cyclic voltammetry (CV) at a constant scan rate of 50 mV s^{-1} (Fig. 5a). Notably, no strong cyclic voltammetry response was observed in the N_2 -saturation KOH electrolyte, whereas the NC@BiOCl-CNTs catalyst had a significant cathodic reduction peak (pacing potential 0.87 V vs. RHE) in the case of O_2 -saturated, higher than the characteristic peak values of C@BiOCl-CNTs and NC@BiOCl catalysts. Subsequently, a similar tendency was detected on the linear sweep voltammeter (LSV) curves (Fig. 5b). The $E_{1/2}$ value of NC@BiOCl-CNTs (0.85 V) differs by 0.1 V from the state-of-the-art noble metal Pt/C catalyst (0.86 V). In particular, the limiting current density of the NC@BiOCl-CNTs catalyst is 5.34 mA cm^{-2} at 0.6 V, which is approximately 1.08-fold higher than that of commercial Pt/C (4.96 mA cm^{-2}). Meanwhile, the NC@BiOCl-CNTs also exhibits significantly superior ORR activity than the N -free C@BiOCl-CNTs, CNTs-free NC@BiOCl, and BiOCl-free N -CNTs (Table S3) and is comparable to most non-noble metal ORR electrocatalysts reported so far (Table S4). Notably, when NC@BiOCl-CNTs was converted to NC@BiOCl-CNTs by immersion in aqua regia, the current density rapidly increased from 4 mA cm^{-2} to 5.34 mA cm^{-2} at 0.6 V, directly indicating that the BiOCl sites enhanced the overall performance of the NC@BiOCl-CNTs catalyst (Fig. S7).

The electron transfer number and H_2O_2 yield of NC@BiOCl-CNTs catalyst were obtained using the RRDE method (Fig. 5c). The results reveal that the H_2O_2 yield is less than 20 % in the potential range of 0.2 to 0.8 V, which is indirect evidence of the four-electron selectivity of the ORR process. Moreover, the NC@BiOCl-CNTs show a Tafel slope of 68.7 mV dec^{-1} (Fig. 5d), which is much lower than C@BiOCl-CNTs (76.2 mV dec^{-1}), NC@BiOCl (85.2 mV dec^{-1}), and N -CNTs (72.1 mV dec^{-1}), verifying fast reaction kinetics [14].

Besides, the LSV measurements (400 to 2025 rpm) at different speeds were also performed (Fig. 5e) [51]. The average electron transfer number was calculated to be 4 from the Koutecky-Levich (K-L) diagram according to the LSV curve in the voltage range of 0.3–0.7 V (inset in Fig. 5e) [52]. The percentage of H_2O_2 and the number of electrons transferred by the catalyst at different potentials are calculated (Fig. 5f). The result is in agreement with that of

the K-L curve. In addition, the charge transfer resistance (R_{ct}) of the highly active NC@BiOCl-CNTs catalyst was lower than those of all control catalysts, as measured by electrochemical impedance spectroscopy (EIS) (Fig. S8), implying a faster electron transfer rate and higher conductivity [53].

The electrochemical double-layer capacitance (C_{dl}) of an electrocatalyst is commonly used to determine its electrochemically active surface area (ECSA) using the polarization curves. The C_{dl} is obtained at different scan rates in the non-Faraday region (Fig. 6a, Figs. S9a–b) [13]. In general, the slope relationship between capacitance current density and scanning rate can be used as a parameter for ECSA demonstration. As depicted in Fig. 6b, the C_{dl} of NC@BiOCl-CNTs catalyst was 16.89 mF cm^{-2} , which was 1.2 and 6.3 times higher than those of C@BiOCl-CNTs (13.62 mF cm^{-2}) and NC@BiOCl (2.7 mF cm^{-2}), respectively, evidencing that NC@BiOCl-CNTs catalyst has a larger ECSA, thereby exposing more accessible active sites [54]. Fig. 6c and Figs. S9c–d shows the linear relationship between the oxidation peak and the scanning rate of the catalyst in KCl solution containing $\text{K}_3(\text{Fe}(\text{CN})_6)$. According to the Randles-Sevcik equation (Fig. 6d) [23], the ECSA of NC@BiOCl-CNTs was 0.71 $\text{m}^2 \text{g}^{-1}$, and 1.4 and 1.5 times higher than those of C@BiOCl-CNTs (0.48 $\text{m}^2 \text{g}^{-1}$) and NC@BiOCl (0.46 $\text{m}^2 \text{g}^{-1}$). This observation is inconsistent with the C_{dl} results.

The methanol crossover tolerance performance of NC@BiOCl-CNTs is investigated by the chronoamperometry (CA) method. Fig. 7a shows that NC@BiOCl-CNTs reveals excellent tolerance to the methanol crossover effect, while the current density of Pt/C drops sharply after injecting methanol into the solution at ca. 200 s. Moreover, the NC@BiOCl-CNTs exhibit long-lasting stability and the current-loss of only 2.5% after 40000 s of operation. On the other hand, the Pt/C current-loss is much greater, about 12.6% (Fig. 7b) under the same conditions [55]. In addition, it is noteworthy that after 2000 CV cycles in succession, the limiting current density of NC@BiOCl-CNTs was slightly decreased by 0.17 mA cm^{-2} , while the limiting current density of Pt/C was significantly decreased by 1.51 mA cm^{-2} (Fig. S10), further reflecting its excellent stability. To study the active sites of highly efficient catalysts, SCN^- was introduced as the masking agent [56]. Fig. 7c shows that the limiting current density and $E_{1/2}$ of NC@BiOCl-CNTs both decrease markedly after the addition of 0.01 M SCN^- . This result indicates that SCN^- binding agents can coordinate with Bi species

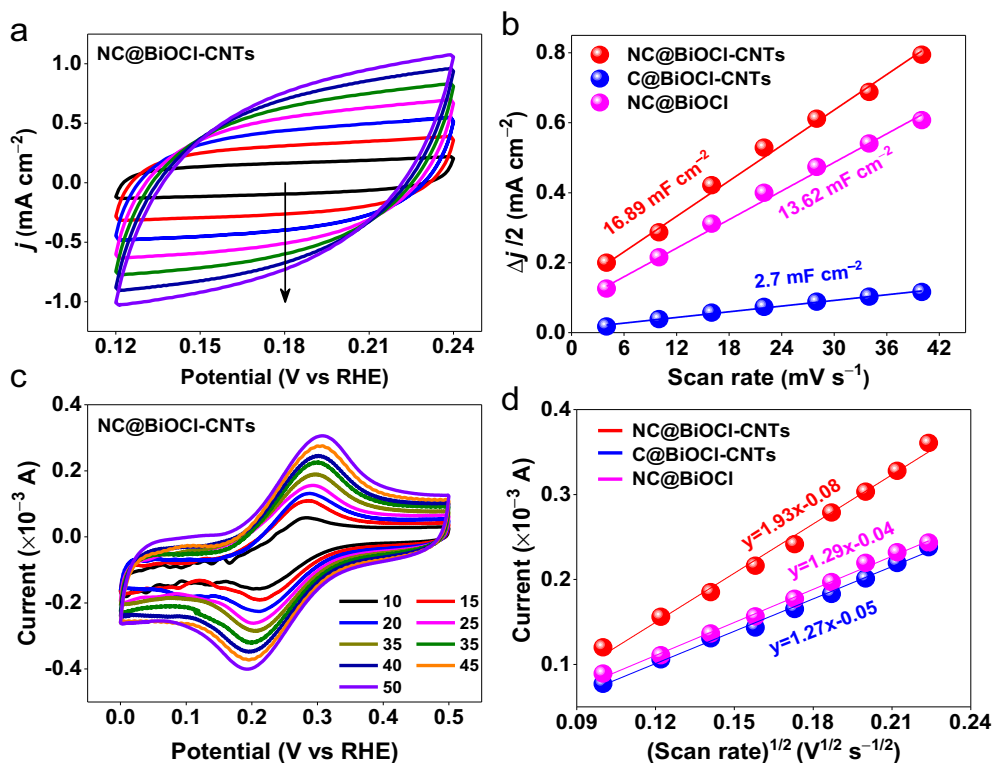


Fig. 6. (a) Cyclic voltammogram curves of NC@BiOCl-CNTs catalyst at scan rates in the range of 4 ~ 40 mV s^{-1} . (b) The summarized C_{dl} values of NC@BiOCl-CNTs, C@BiOCl-CNTs and NC@BiOCl. (c) CV responses of NC@BiOCl-CNTs catalyst in 0.1 M KCl containing 5 mM $\text{K}_3[\text{Fe}(\text{CN})_6]$ solution as a function of scan rate from 10 to 50 mV s^{-1} . (d) Linear relationship of peak current versus square root of scan rates for NC@BiOCl-CNTs, C@BiOCl-CNTs and NC@BiOCl, respectively.

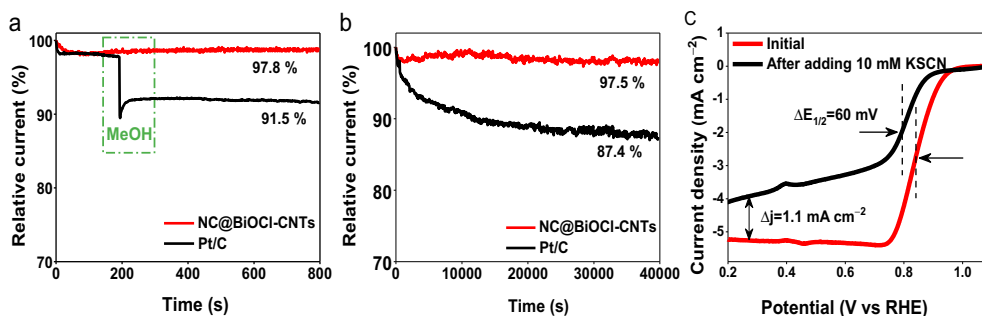


Fig. 7. (a) Methanol crossover tolerance measurement of NC@BiOCl-CNTs and 20 wt% Pt/C in 0.1 M KOH with the addition of 3.0 M methanol at ca. 200 s. (b) Chronoamperometric response of NC@BiOCl-CNTs and 20 wt% Pt/C at 0.65 V (vs. RHE) with 1600 rpm for 40000 s. (c) The LSV polarization curves of NC@BiOCl-CNTs catalyst before and after adding 0.01 M SCN^- with a rotate speed of 1600 rpm.

to form a stable coordination compound, which decreases the ORR performance of the catalyst [2,57].

3.5. Zinc-air battery study

Finally, a zinc-air battery with NC@BiOCl-CNTs as the air-cathode was constructed to explore the practical application of energy devices, as displayed in Fig. 8a. The NC@BiOCl-CNTs-based and benchmark Pt/C-based battery exhibits a platform voltage of 1.25 and 1.17 V (Fig. 8b). Also, the NC@BiOCl-CNTs-based system delivers the specific capacities of 724 mAh g^{-1} at a discharge current density of 10 mA cm^{-2} , outperforming the battery assembled by Pt-based catalyst [58]. The discharge voltage and power density are presented in Fig. 8c, NC@BiOCl-CNTs battery provides a power density of 170.7 mW cm^{-2} , far exceeding that of Pt/C (129.6 mW cm^{-2}) and most pre-

viously reported systems (Table S5). NC@BiOCl-CNTs catalyst affords a stable open-circuit voltage of about 1.51 V in comparison with that of the commercial Pt/C (Fig. 8d). Likewise, the NC@BiOCl-CNTs battery in series can illuminate the red light-emitting diode (LED) with the required 3.0 V voltage (Fig. 8e). As shown in Fig. 8f, NC@BiOCl-CNTs catalyst maintains a relatively stable discharge capacity at different current densities. Notable, the platform voltage was also restored to 1.27 V when the discharge current density was restored to 2 mA cm^{-2} , indicating good reversibility based on the rechargeable zinc-air battery. In Fig. 8g-h, the stability of NC@BiOCl-CNTs is also evaluated by cyclic durability and rechargeability. After 155 h of long-term operation, the NC@BiOCl-CNTs-based battery does not show any evidence of voltage drop, exhibiting excellent cycle stability compared to the commercial Pt/C. The high potential for NC@BiOCl-CNTs as an

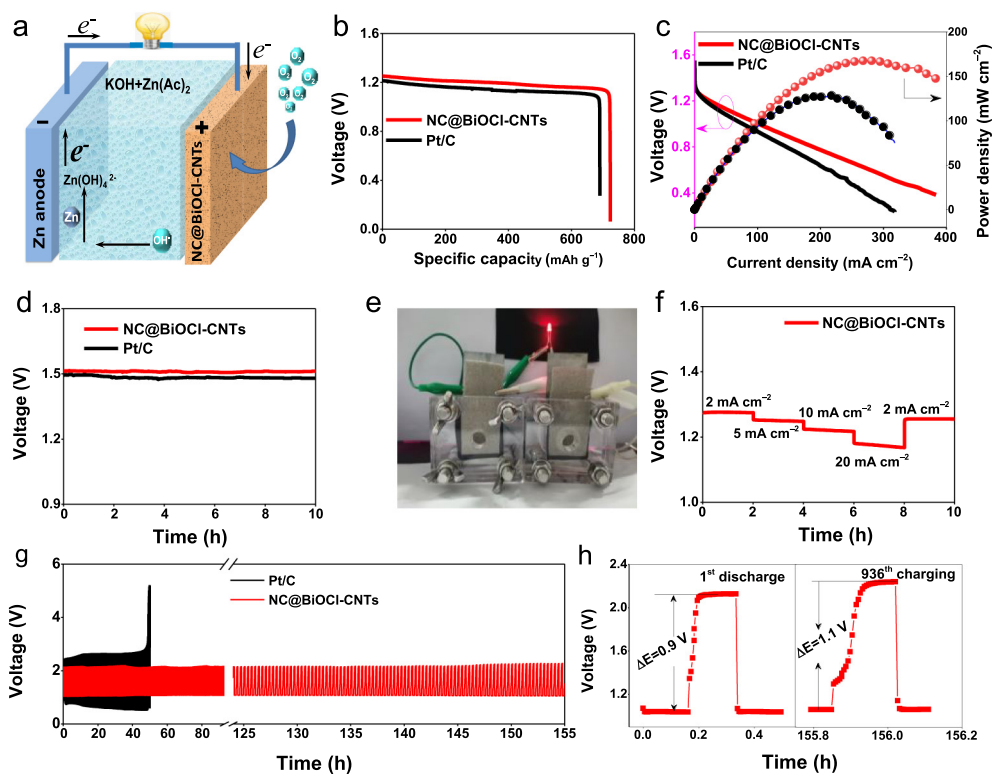


Fig. 8. (a) Structural diagram of assembled rechargeable Zn–air batteries. (b) Specific capacities plots at 10 mA cm^{-2} for NC@BiOCl-CNTs and 20 wt% Pt/C. (c) Discharge polarization and power density curves of NC@BiOCl-CNTs as air-cathode. (d) Open-circuit plots of Zn–air batteries using Pt/C and NC@BiOCl-CNTs as ORR catalysts in aqueous solution. (e) Red LED photo powered in series by two sets of Zn–air batteries. (f) Galvanostatic discharge at different current densities. (g, h) Galvanostatic discharge and charge voltage profiles of the rechargeable Zn–air batteries at 5 mA cm^{-2} (10 min for each cycle).

electrocatalyst for oxygen reduction is further demonstrated by a comprehensive comparison with noble metal Pt/C catalyst, making it more competitive in practical applications.

4. Conclusion

In summary, nanostructured NC-meshed BiOCl particles were successfully prepared via a feasible strategy for the first time. N-doped carbon encapsulation on metal nanocatalysts not only ensures high conductivity but also prevents the catalyst aggradation. The NC@BiOCl-CNTs catalyst displayed excellent ORR activity compared with commercial Pt/C in 0.1 M KOH solution. Most importantly, the NC@BiOCl-CNTs catalyst coupled with large ECSA and relatively short diffusion lengths. In addition, the Zn–air batteries using NC@BiOCl-CNTs catalyst as an air cathode have a highly competitive peak power density (170.7 mW cm^{-2}) and can cycle stably for >155 h at 10 mA cm^{-2} . This work may open a new path for the rational design of highly active ORR electrocatalysts.

CRediT authorship contribution statement

Xue Shao: Investigation, Methodology. **Yuting Yang:** Investigation, Data curation. **Yi Liu:** Data curation. **Puxuan Yan:** Methodology. **Shuqing Zhou:** Data curation. **Tayirjan Taylor Isimjan:** Writing–review & editing. **Xiulin Yang:** Supervision, Writing–review & editing.

Declaration of Competing Interest

The authors declare that they have no known competing financial interests or personal relationships that could have appeared to influence the work reported in this paper.

Acknowledgments

This work has been supported by the National Natural Science Foundation of China (no. 21965005), Natural Science Foundation of Guangxi Province (2018GXNSFAA294077, 2021GXNSFAA076001), Project of High-Level Talents of Guangxi (F-KA18015), and Guangxi Technology Base and Talent Subject (GUIKE AD18126001, GUIKE AD20297039).

Appendix A. Supplementary material

Supplementary data to this article can be found online at <https://doi.org/10.1016/j.jcis.2021.08.210>.

References

- [1] S. Liu, Z. Li, C. Wang, W. Tao, M. Huang, M. Zuo, Y. Yang, K. Yang, L. Zhang, S. Chen, P. Xu, Q. Chen, Turning main-group element magnesium into a highly active electrocatalyst for oxygen reduction reaction, *Nat. Commun.* 11 (2020) 938.
- [2] H. Ye, L. Li, D. Liu, Q. Fu, F. Zhang, P. Dai, X. Gu, X. Zhao, Sustained-Release Method for the Directed Synthesis of ZIF-Derived Ultrafine Co-N-C ORR Catalysts with Embedded Co Quantum Dots, *ACS Appl. Mater. Interfaces* 12 (2020) 57847–57858.
- [3] M. Xiao, Z. Xing, Z. Jin, C. Liu, J. Ge, J. Zhu, Y. Wang, X. Zhao, Z. Chen, Preferentially Engineering FeN₄ Edge Sites onto Graphitic Nanosheets for Highly Active and Durable Oxygen Electrocatalysis in Rechargeable Zn–Air Batteries, *Adv. Mater.* 32 (2020) 2004900.
- [4] J.-S. Lee, S. Tai Kim, R. Cao, N.-S. Choi, M. Liu, K.T. Lee, J. Cho, Metal-Air Batteries with High Energy Density: Li–Air versus Zn–Air, *Adv. Energy Mater.* 1 (2011) 34–50.
- [5] J. Fu, R. Liang, G. Liu, A. Yu, Z. Bai, L. Yang, Z. Chen, Recent Progress in Electrically Rechargeable Zinc-Air Batteries, *Adv. Mater.* 31 (2019) 1805230.
- [6] D.C. Nguyen, D.T. Tran, T.L.L. Doan, D.H. Kim, N.H. Kim, J.H. Lee, Rational Design of Core@shell Structured CoS_x@Cu₂MoS₄ Hybridized MoS₂/N, S-Codoped Graphene as Advanced Electrocatalyst for Water Splitting and Zn-Air Battery, *Adv. Energy Mater.* 10 (2020) 1903289.

- [7] H. Yang, L. Gong, H. Wang, C. Dong, J. Wang, K. Qi, H. Liu, X. Guo, B.Y. Xia, Preparation of nickel-iron hydroxides by microorganism corrosion for efficient oxygen evolution, *Nat. Commun.* 11 (2020) 5075.
- [8] T. Wang, Y. He, Y. Liu, F. Guo, X. Li, H. Chen, H. Li, Z. Lin, A ZIF-triggered rapid polymerization of dopamine renders Co/N-codoped cage-in-cage porous carbon for highly efficient oxygen reduction and evolution, *Nano Energy* 79 (2021) 105487.
- [9] G. Liu, J. Li, J. Fu, G. Jiang, G. Lui, D. Luo, Y.P. Deng, J. Zhang, Z.P. Cano, A. Yu, D. Su, Z. Bai, L. Yang, Z. Chen, An Oxygen-Vacancy-Rich Semiconductor-Supported Bifunctional Catalyst for Efficient and Stable Zinc-Air Batteries, *Adv. Mater.* 31 (2019) 1806761.
- [10] Z. Liang, H.Y. Wang, H. Zheng, W. Zhang, R. Cao, Porphyrin-based frameworks for oxygen electrocatalysis and catalytic reduction of carbon dioxide, *Chem. Soc. Rev.* 50 (2021) 2540–2581.
- [11] M. Luo, W. Sun, B.B. Xu, H. Pan, Y. Jiang, Interface Engineering of Air Electrocatalysts for Rechargeable Zinc-Air Batteries, *Adv. Energy Mater.* 11 (2020) 2002762.
- [12] T. Tang, W.J. Jiang, X.Z. Liu, J. Deng, S. Niu, B. Wang, S.F. Jin, Q. Zhang, L. Gu, J.S. Hu, L.J. Wan, Metastable Rock Salt Oxide-Mediated Synthesis of High-Density Dual-Protected M@NC for Long-Life Rechargeable Zinc-Air Batteries with Record Power Density, *J. Am. Chem. Soc.* 142 (2020) 7116–7127.
- [13] R. Zhao, Q. Li, Z. Chen, V. Jose, X. Jiang, G. Fu, J.-M. Lee, S. Huang, B. N-doped ultrathin carbon nanosheet superstructure for high-performance oxygen reduction reaction in rechargeable zinc-air battery, *Carbon* 164 (2020) 398–406.
- [14] Y. Wang, N. Xu, R. He, L. Peng, D. Cai, J. Qiao, Large-scale defect-engineering tailored tri-doped graphene as a metal-free bifunctional catalyst for superior electrocatalytic oxygen reaction in rechargeable Zn-air battery, *Appl. Catal. B: Environ.* 285 (2021) 119811.
- [15] S. Huang, Y. Meng, Y. Cao, S. He, X. Li, S. Tong, M. Wu, N⁻, O⁻ and P-doped hollow carbons: Metal-free bifunctional electrocatalysts for hydrogen evolution and oxygen reduction reactions, *Appl. Catal. B: Environ.* 248 (2019) 239–248.
- [16] J. Qin, Z. Liu, D. Wu, J. Yang, Optimizing the electronic structure of cobalt via synergized oxygen vacancy and Co-N-C to boost reversible oxygen electrocatalysis for rechargeable Zn-air batteries, *Appl. Catal. B: Environ.* 278 (2020) 119300.
- [17] L. Huang, S. Zaman, X. Tian, Z. Wang, W. Fang, B.Y. Xia, Advanced Platinum-Based Oxygen Reduction Electrocatalysts for Fuel Cells, *Acc. Chem. Res.* 54 (2021) 311–322.
- [18] D. Chen, J. Zhu, X. Mu, R. Cheng, W. Li, S. Liu, Z. Pu, C. Lin, S. Mu, Nitrogen-Doped carbon coupled FeNi₃ intermetallic compound as advanced bifunctional electrocatalyst for OER, ORR and Zn-air batteries, *Appl. Catal. B: Environ.* 268 (2020) 118729.
- [19] Q. Lu, J. Yu, X. Zou, K. Liao, P. Tan, W. Zhou, M. Ni, Z. Shao, Self-Catalyzed Growth of Co, N-Codoped CNTs on Carbon-Encased Co_x Surface: A Noble-Metal-Free Bifunctional Oxygen Electrocatalyst for Flexible Solid Zn-Air Batteries, *Adv. Funct. Mater.* 29 (2019) 1904481.
- [20] C. Tang, H.F. Wang, Q. Zhang, Multiscale Principles To Boost Reactivity in Gas-Involving Energy Electrocatalysis, *Acc. Chem. Res.* 51 (2018) 881–889.
- [21] D. Alba-Molina, A.R. Puentes Santiago, J.J. Giner-Casares, E. Rodríguez-Castellón, M.T. Martín-Romero, L. Camacho, R. Luque, M. Cano, Correction: Tailoring the ORR and HER electrocatalytic performances of gold nanoparticles through metal-ligand interfaces, *J. Mater. Chem. A* 7 (2019) 20435.
- [22] L. Yan, Z. Xu, W. Hu, J. Ning, Y. Zhong, Y. Hu, Formation of sandwiched leaf-like CNTs-Co/ZnCo₂O₄@NC-CNTs nanohybrids for high-power-density rechargeable Zn-air batteries, *Nano Energy* 82 (2021) 105710.
- [23] M. Qian, M. Xu, S. Zhou, J. Tian, T. Taylor Isimjan, Z. Shi, X. Yang, Template synthesis of two-dimensional ternary nickel-cobalt-nitrogen co-doped porous carbon film: Promoting the conductivity and more active sites for oxygen reduction, *J. Colloid Interface Sci.* 564 (2020) 276–285.
- [24] M.-A. Légaré, G. Bélanger-Chabot, R.D. Dewhurst, E. Welz, I. Krummenacher, B. Engels, H. Braunschweig, Nitrogen fixation and reduction at boron, *Science* 359 (2018) 896–900.
- [25] E. Zhang, T. Wang, K. Yu, J. Liu, W. Chen, A. Li, H. Rong, R. Lin, S. Ji, X. Zheng, Y. Wang, L. Zheng, C. Chen, D. Wang, J. Zhang, Y. Li, Bismuth Single Atoms Resulting from Transformation of Metal-Organic Frameworks and Their Use as Electrocatalysts for CO₂ Reduction, *J. Am. Chem. Soc.* 141 (2019) 16569–16573.
- [26] W. Ouyang, F. Teng, X. Fang, High Performance BiOCl Nanosheets/TiO₂ Nanotube Arrays Heterojunction UV Photodetector: The Influences of Self-Induced Inner Electric Fields in the BiOCl Nanosheets, *Adv. Funct. Mater.* 28 (2018) 1707178.
- [27] R. Kashfi-Sadabad, S. Yazdani, T.D. Huan, Z. Cai, M.T. Pettes, Role of Oxygen Vacancy Defects in the Electrocatalytic Activity of Substoichiometric Molybdenum Oxide, *J. Phys. Chem. C* 122 (2018) 18212–18222.
- [28] M. Zorko, P. Farinazzo Bergamo Dias Martins, J.G. Connell, P.P. Lopes, N.M. Markovic, V.R. Stamenkovic, D. Strmcnik, Improved Rate for the Oxygen Reduction Reaction in a Sulfuric Acid Electrolyte using a Pt(111) Surface Modified with Melamine, *ACS Appl. Mater. Interfaces* 13 (2021) 3369–3376.
- [29] L. Feng, T. Wang, H. Sun, M. Jiang, Y. Chen, Carbon Nitride Anchored on a Nitrogen-Doped Carbon Nanotube Surface for Enhanced Oxygen Reduction Reaction, *ACS Appl. Mater. Interfaces* 12 (2020) 56954–56962.
- [30] H. Jiang, L. Wang, Y. Li, B. Gao, Y. Guo, C. Yan, M. Zhuo, H. Wang, S. Zhao, High-selectivity electrochemical CO₂ reduction to formate at low overpotential over Bi catalyst with hexagonal sheet structure, *Appl. Surf. Sci.* 541 (2021) 148577.
- [31] X. Cheng, P. Yan, S. Liu, M. Qian, B. Wang, Z. Wan, J. Tian, X.-C. Shen, T.T. Isimjan, X. Yang, Well-dispersed iron oxide stabilized Fe-N₄ active sites in porous N-doped carbon spheres as alternative superior catalyst for oxygen reduction, *Int. J. Hydrogen Energy* 44 (2019) 12127–12137.
- [32] M. Li, S. Yu, H. Huang, X. Li, Y. Feng, C. Wang, Y. Wang, T. Ma, L. Guo, Y. Zhang, Unprecedented Eighteen-Faceted BiOCl with a Ternary Facet Junction Boosting Cascade Charge Flow and Photo-redox, *Angew. Chem. Int. Ed.* 58 (2019) 9517–9521.
- [33] X. Cheng, S. Dou, G. Qin, B. Wang, P. Yan, T.T. Isimjan, X. Yang, Rational design of highly selective nitrogen-doped Fe₂O₃-CNTs catalyst towards H₂O₂ generation in alkaline media, *Int. J. Hydrogen Energy* 45 (2020) 6128–6137.
- [34] A. Gupta, S.R. Dhakate, P. Pal, A. Dey, P.K. Iyer, D.K. Singh, Effect of graphitization temperature on structure and electrical conductivity of polyacrylonitrile based carbon fibers, *Diamond Relat. Mater.* 78 (2017) 31–38.
- [35] J. Zhao, Y. Liu, X. Quan, S. Chen, H. Yu, H. Zhao, Nitrogen-doped carbon with a high degree of graphitization derived from biomass as high-performance electrocatalyst for oxygen reduction reaction, *Appl. Surf. Sci.* 396 (2017) 986–993.
- [36] S. Gadipelli, T. Zhao, S.A. Shevlin, Z. Guo, Switching effective oxygen reduction and evolution performance by controlled graphitization of a cobalt–nitrogen–carbon framework system, *Energy Environ. Sci.* 9 (2016) 1661–1667.
- [37] S. Chen, L. Zhao, J. Ma, Y. Wang, L. Dai, J. Zhang, Edge-doping modulation of N, P-codoped porous carbon spheres for high-performance rechargeable Zn-air batteries, *Nano Energy* 60 (2019) 536–544.
- [38] S. Dou, S. Zhou, H. Huang, P. Yan, E. Shoko, T.T. Isimjan, X. Yang, Metal-Organic Framework (MOF)-Derived Electron-Transfer Enhanced Homogeneous PdO-Rich Co₃O₄ as a Highly Efficient Bifunctional Catalyst for Sodium Borohydride Hydrolysis and 4-Nitrophenol Reduction, *Chem. Eur. J.* 26 (2020) 16923–16931.
- [39] S. Dou, W. Zhang, Y. Yang, S. Zhou, X. Rao, P. Yan, T.T. Isimjan, X. Yang, Shaggy-like Ru-clusters decorated core-shell metal-organic framework-derived CoO_x@NPC as high-efficiency catalyst for NaBH₄ hydrolysis, *Int. J. Hydrogen Energy* 46 (2021) 7772–7781.
- [40] R. Rameshbabu, M. Sandhiya, G. Pecchi, M. Sathish, Effective coupling of Cu (II) with BiOCl nanosheets for high performance electrochemical supercapacitor and enhanced photocatalytic applications, *Appl. Surf. Sci.* 521 (2020) 146362.
- [41] S. Abednatanzi, P. Gohari Derakhshandeh, K. Leus, H. Vrielinck, F. Callens, J. Schmidt, A. Savateev, P. Van Der Voort, Metal-free activation of molecular oxygen by covalent triazine frameworks for selective aerobic oxidation, *Sci. Adv.* 6 (2020) 2310.
- [42] M. Qian, X. Cheng, T. Sun, J. Tian, T.T. Isimjan, Z. Shi, X. Yang, Synergistic catalytic effect of N-doped carbon embedded with CoFe-rich CoFe₂O₄ clusters as highly efficient catalyst towards oxygen reduction, *J. Alloys Compd.* 819 (2020) 153015.
- [43] X. Ning, Y. Li, J. Ming, Q. Wang, H. Wang, Y. Cao, F. Peng, Y. Yang, H. Yu, Electronic synergism of pyridinic- and graphitic-nitrogen on N-doped carbons for the oxygen reduction reaction, *Chem. Sci.* 10 (2019) 1589–1596.
- [44] P. Yan, J. Liu, S. Yuan, Y. Liu, W. Cen, Y. Chen, The promotion effects of graphitic and pyridinic N combinational doping on graphene for ORR, *Appl. Surf. Sci.* 445 (2018) 398–403.
- [45] T. Jia, J. Wu, Z. Ji, C. Peng, Q. Liu, M. Shi, J. Zhu, H. Wang, D. Liu, M. Zhou, Surface defect engineering of Fe-doped Bi₂O₃ microflowers for ameliorating charge-carrier separation and molecular oxygen activation, *Appl. Catal. B: Environ.* 284 (2021) 119727.
- [46] P. Yan, M. Huang, B. Wang, Z. Wan, M. Qian, H. Yan, T.T. Isimjan, J. Tian, X. Yang, Oxygen defect-rich double-layer hierarchical porous Co₃O₄ arrays as high-efficient oxygen evolution catalyst for overall water splitting, *J. Energy Chem.* 47 (2020) 299–306.
- [47] C. Tomon, A. Krittayavathananon, S. Sarawutanukul, S. Duangdangchote, N. Phattarasupakun, K. Homlamai, M. Sawangphruk, Enhancing bifunctional electrocatalysts of hollow Co₃O₄ nanorods with oxygen vacancies towards ORR and OER for Li–O₂ batteries, *Electrochim. Acta* 367 (2021) 137490.
- [48] M.-C. Tsai, T.-T. Nguyen, N.G. Akalework, C.-J. Pan, J. Rick, Y.-F. Liao, W.-N. Su, B.-J. Hwang, Interplay between Molybdenum Dopant and Oxygen Vacancies in a TiO₂ Support Enhances the Oxygen Reduction Reaction, *ACS Catal.* 6 (2016) 6551–6559.
- [49] L. Yi, J. Chen, P. Shao, J. Huang, X. Peng, J. Li, G. Wang, C. Zhang, Z. Wen, Molten-Salt-Assisted Synthesis of Bismuth Nanosheets for Long-term Continuous Electrocatalytic Conversion of CO₂ to Formate, *Angew. Chem. Int. Ed.* 59 (2020) 20112–20119.
- [50] J. Zhu, J. Fan, T. Cheng, M. Cao, Z. Sun, R. Zhou, L. Huang, D. Wang, Y. Li, Y. Wu, Bilayer nanosheets of unusual stoichiometric bismuth oxychloride for potassium ion storage and CO₂ reduction, *Nano Energy* 75 (2020) 104939.
- [51] Z. Liang, X. Fan, H. Lei, J. Qi, Y. Li, J. Gao, M. Huo, H. Yuan, W. Zhang, H. Lin, H. Zheng, R. Cao, Cobalt-Nitrogen-Doped Helical Carbonaceous Nanotubes as a Class of Efficient Electrocatalysts for the Oxygen Reduction Reaction, *Angew. Chem. Int. Ed.* 57 (2018) 13187–13191.
- [52] J. Lilloja, E. Kibena-Pöldsepp, A. Sarapu, M. Kodali, Y. Chen, T. Asset, M. Käärik, M. Merisal, P. Paiste, J. Aruväli, A. Treshchalov, M. Rähn, J. Leis, V. Sammelseg, S. Holdcroft, P. Atanassov, K. Tammeveski, Cathode Catalysts Based on Cobalt- and Nitrogen-Doped Nanocarbon Composites for Anion Exchange Membrane Fuel Cells, *ACS Appl. Energy Mater.* 3 (2020) 5375–5384.
- [53] B. Huang, X. Zhang, J. Cai, W. Liu, S. Lin, A novel MnO₂/rGO composite prepared by electrodeposition as a non-noble metal electrocatalyst for ORR, *J. Appl. Electrochem.* 49 (2019) 767–777.

- [54] X.L. Wang, L.Z. Dong, M. Qiao, Y.J. Tang, J. Liu, Y. Li, S.L. Li, J.X. Su, Y.Q. Lan, Exploring the Performance Improvement of the Oxygen Evolution Reaction in a Stable Bimetal–Organic Framework System, *Angew. Chem. Int. Ed.* 57 (2018) 9660–9664.
- [55] J. Wang, W. Zang, S. Xi, M. Kosari, S.J. Pennycook, H.C. Zeng, Trimetal atoms confined in openly accessible nitrogen-doped carbon constructs for an efficient ORR, *J. Mater. Chem. A* 8 (2020) 17266–17275.
- [56] Y. Cheng, J. Zhang, S.P. Jiang, Are metal-free pristine carbon nanotubes electrocatalytically active?, *Chem Commun.* 51 (2015) 13764–13767.
- [57] Y. Wang, K. Qi, S. Yu, G. Jia, Z. Cheng, L. Zheng, Q. Wu, Q. Bao, Q. Wang, J. Zhao, X. Cui, W. Zheng, Revealing the Intrinsic Peroxidase-Like Catalytic Mechanism of Heterogeneous Single-Atom Co–MoS₂, *Nano-Micro Lett.* 11 (2019) 102.
- [58] A. Kraytsberg, Y. Ein-Eli, The impact of nano-scaled materials on advanced metal–air battery systems, *Nano Energy* 2 (2013) 468–480.